J. Fluid Mech. (1974), *vol.* 66, *part* 3, *pp.* 481–505
Printed in Great Britain

A boundary layer developing in an increasingly adverse pressure gradient

By A. E. SAMUEL AND P. N. JOUBERT
Department of Mechanical Engineering, University of Melbourne

(Received 7 March 1972 and in revised form 2 May 1974)

This paper deals with a survey of mean flow and fluctuating quantities in a turbulent boundary layer developing on a smooth wall in a pressure domain $P(x)$, where both dP/dx and d^2P/dx^2 are positive (increasingly adverse). The two-dimensional nature of the flow field was checked by momentum balance, as well as velocity traverses either side of the working section centre-line. Using the integrated form of the momentum integral equation, it was found that the skin-friction term and the summed momentum and pressure terms differed by at most 19%; but for the majority of measuring points they differed by less than 14%. The off-centre-line velocity profiles were indistinguishable from those taken on the centre-line. The flow field was also surveyed for fluctuating components $(\overline{u_1^2})^{\frac{1}{2}}$, $(\overline{u_2^2})^{\frac{1}{2}}$, $(\overline{u_3^2})^{\frac{1}{2}}$ and $\overline{u_1 u_2}$, as well as for u_1 spectra. Wherever possible, the results were compared with existing models of boundary-layer development. These comparisons indicated that the only all-embracing model for boundary-layer development is the law of the wall.

1. Introduction

At the Stanford conference on computation of turbulent boundary layers (Kline, Morkovin, Sovran & Cockrell 1968) more than fifty leading workers in turbulent boundary layers met to compare available models for boundary-layer development. One of the main conclusions of the conference is summed up in the report of the evaluating committee: "Conclusion no. 23. It is critically important to continuously obtain new and better data. Without new data someone will get 'perfect' agreement with the mandatory flows by the simple expedience of introducing a suitable number of arbitrary 'correlation' functions and parameters."

Work has continued at the University of Melbourne collecting such information in a variety of situations, since 1959. Because adverse pressure gradient flows are easiest to set up in a straight-walled diffuser, most experiments were conducted with this type of geometry, as was the case with most other workers. But such straight walls give a decreasingly adverse pressure gradient distribution in the streamwise direction. For the majority of cases where adjustable flow geometry was used (e.g. Clauser 1954; Stratford 1959*a*, *b*; Moses 1964), measurements again were taken where the pressure gradient was decreasingly adverse ($dP/dx > 0$, $d^2P/dx^2 < 0$).

Sandborn & Slogar (1955) collected detailed measurements of a turbulent boundary layer developing in adverse pressure gradients. Only at the first two of their few measuring stations was the pressure gradient increasingly adverse, and consequently the development behaviour in such a gradient could not be deduced. To the best of the authors' knowledge, Sandborn & Slogar's measurements are the only ones collected in the increasingly adverse pressure gradient.

There are many real flow situations (such as on ship hulls, aircraft wings and bodies of revolution), where part of the streamwise pressure gradient distribution is increasingly adverse (see e.g. Goldstein 1965, pp. 404, 405, 525, where measured pressure distributions on aerofoils and airship hulls are presented). An increasingly adverse pressure gradient distribution is also observed on many of the wing sections presented by Abbott & Von Doenhoff (1949).

This paper is concerned with measurements taken in a two-dimensional boundary layer developing in this experimentally neglected pressure domain where dP/dx and d^2P/dx^2 are both positive (increasingly adverse pressure gradient distribution). To some extent, it is also concerned with finding appropriate models to represent flow development in an increasingly adverse gradient layer. For this purpose, only models based on sound physical hypotheses (as opposed to purely empirical models) were used in comparing predicted with observed flow phenomena.

The experiment was set up in a flexible-roof boundary-layer tunnel, built in 1965 after the style of Bradshaw (1965). It was hoped that this tunnel would allow the construction of finely controlled streamwise pressure distributions, as well as possess a greater aspect ratio (and hence better two-dimensionality) in the working section. For further details about the tunnel and some preliminary test data on tunnel performance, the reader may refer to Holt (1969).

2. The experiment

The work was performed at the University of Melbourne in a return circuit boundary-layer tunnel, with a $1 \times 0{\cdot}36$ m inlet to the working section. The reference Reynolds number measured upstream of the inlet was kept approximately constant at $1{\cdot}7 \times 10^6$ m^{-1} throughout the experiment. All streamwise (x) measurements are given relative to the position of the first wall pressure tap ($x = 0$). The layer was tripped by 32 mm diameter pins, 25 mm high, placed in a row with a 64 mm centre spacing at a position $x = 161$ mm.

The first stage of the experiment involved accurate measurement of the pressure gradient distribution along the tunnel centre-line. Experimental procedure and reduction of results follow the method outlined by Perry, Schofield & Joubert (1969). Figure 1 shows the probe and traversing mechanism used. A Chattock manometer was used for all pressure difference measurements, with a sensitivity of 0·01 mm H_2O.

Mean velocity profiles were measured using a boundary-layer probe, with a flattened total head tube and a separate local static tube. The geometry of the total head tube and a diagrammatic view of the boundary-layer probe are both shown in figure 2. Several complete mean velocity profile measurements were

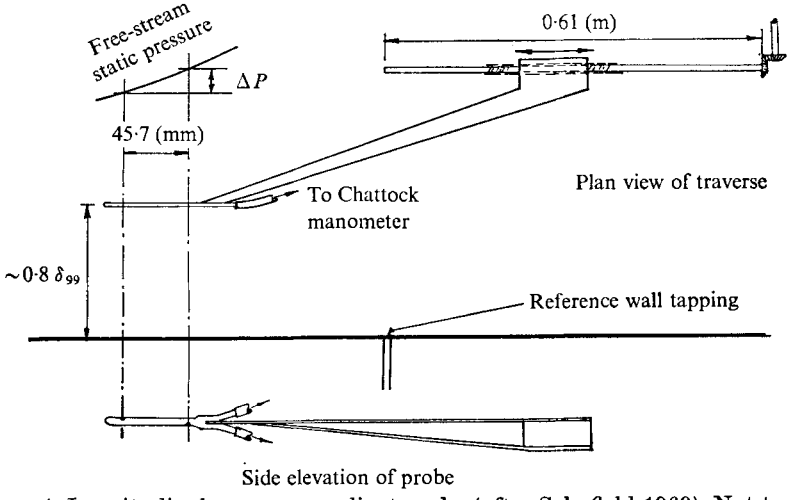

FIGURE 1. Longitudinal pressure gradient probe (after Schofield 1969). Not to scale.

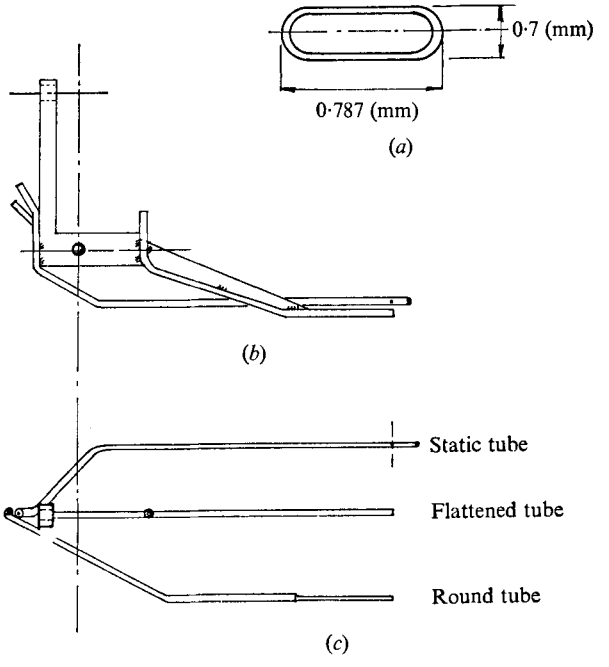

FIGURE 2. Boundary-layer probe. Not to scale. (*a*) End view of flattened total head tube. (*b*) Side elevation of probe. (*c*) Plan view of probe.

repeated, using a round total head tube with a frontal area approximately equal to the flattened tube, and the two sets of results were indistinguishable. The automatic traversing and recording system was calibrated against a standard NPL Pitot-static tube. Agreement between calibration and standard was better than $\frac{1}{2}\%$.

Wall shear stress measurements were made using Preston tubes, with Patel's

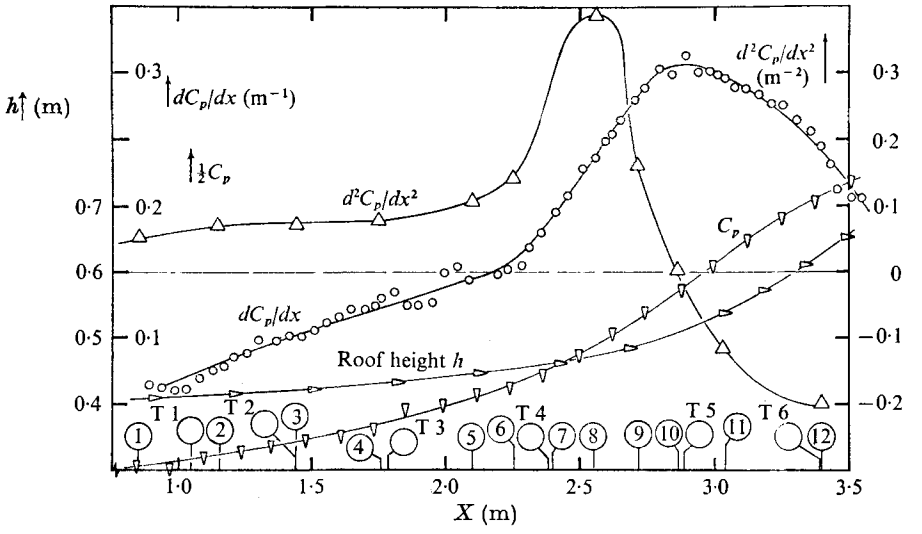

FIGURE 3. Flow field parameters.

(1965) calibration data, as well as the floating element shear stress meter of Brown & Joubert (1969). Agreement between these measurements and the estimated wall shear stress from the mean flow velocity profiles was excellent.

Fluctuating velocity components and Reynolds stresses were measured with a constant-temperature hot-wire anemometer. Both normal and inclined wire probes were calibrated using dynamic calibration procedures developed by Perry & Morrison (1971*a*) and Morrison, Perry & Samuel (1972).

These direct calibration procedures do not require a static calibration plot for determining dE/dU, the dynamic sensitivity of the hot wire to fluctuations in velocity U. Consequently, mean velocity profiles were not needed when using the hot-wire anemometer. As most profiles were established in regions of high velocity, where hot-wire anemometers are increasingly inaccurate for mean velocity measurement, only Pitot measurements of mean velocity are presented.

3. The mean flow

This section deals with the results and discussion of mean flow measurements.

Figure 3 shows the various parameters associated with the boundary layer under study. The layer develops in an increasingly adverse streamwise pressure gradient between stations 1 and 10, and after that becomes decreasingly adverse. The graph C_p against x was drawn from readings taken from static tappings on the centre-line of the tunnel floor; the graph of dC_p/dx from a special probe; the graph of d^2C_p/dx^2 by differentiation of the smoothed dC_p/dx curve. (Density ρ; reference velocity U_{∞_0}; $C_p = 2[P(x)-P(x_0)]/\rho U^2_{\infty_0}$.)

The mean velocity profile plots are shown on figures 4 (*a*) and (*b*). Semi-logarithmic axes have been used, and the lines shown are Clauser lines obtained from

$$U/U_\tau = 1/0{\cdot}4 \log_e (yU_\tau/\nu) + 5{\cdot}1,$$

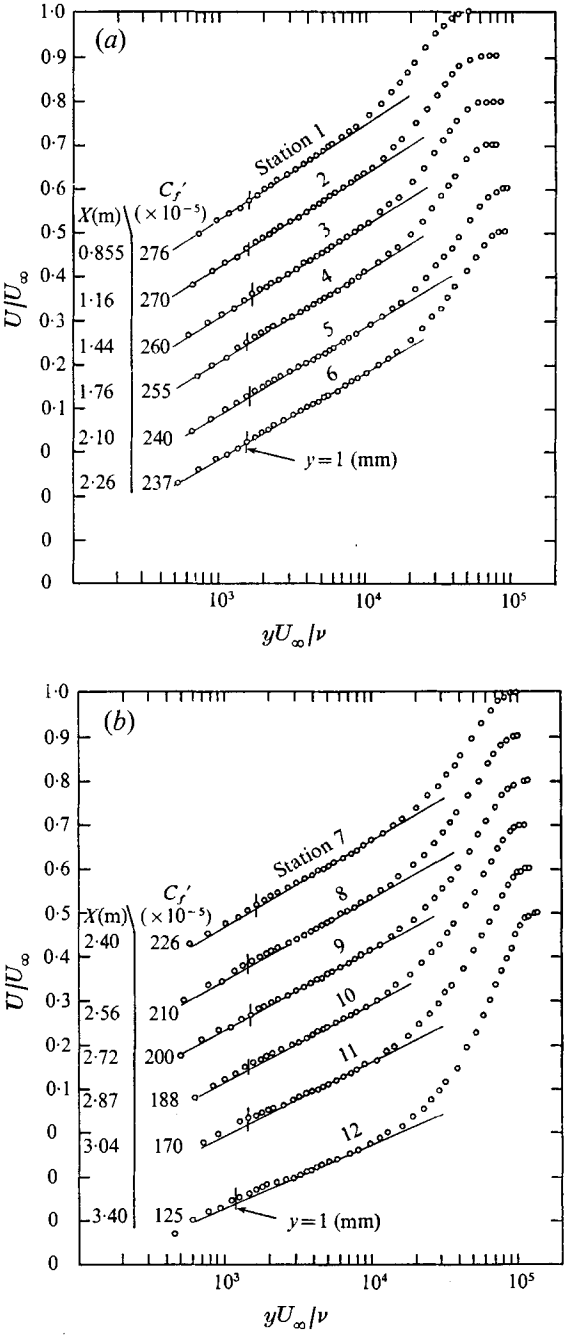

FIGURE 4. Mean velocity profiles. $C_f' = 2\tau_0/\rho U_\infty$. ○, measurement; ——, Clauser lines ($\kappa = 0{\cdot}4$, $A = 5{\cdot}1$).

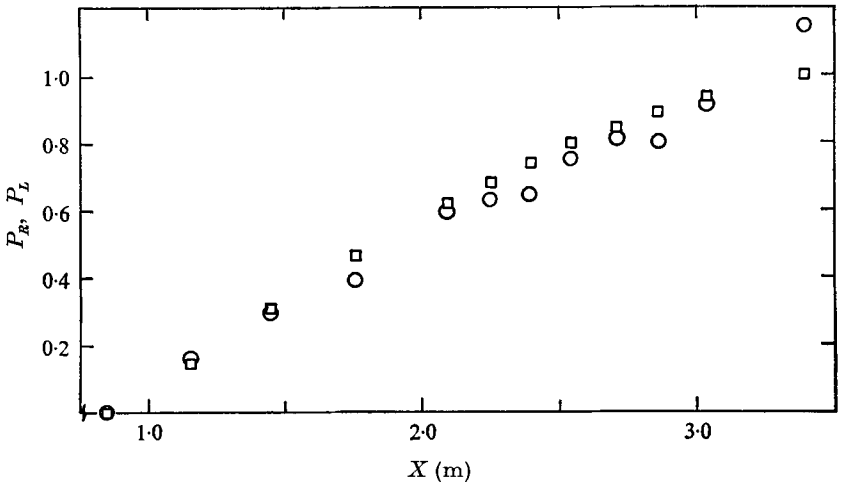

FIGURE 5. Momentum balance. □, P_R; ○, P_L.

where $U_\tau = (\tau_0/\rho)^{\frac{1}{2}}$, for wall shear stress τ_0, kinematic viscosity ν and local mean velocity U at a distance y from the wall.

To check the two-dimensionality of the layer, a momentum balance was carried out. Using the notation of Coles & Hirst (1968), the results are plotted as P_L and P_R against downstream distance x.

$$P_L = \frac{U_\infty^2 \theta}{U_{\infty_0}^2 \theta_0} - 1 + \int_{x_0}^{x} \frac{U_\infty \delta^* dU_\infty}{U_\infty^2 \theta_0} dx,$$

$$P_R = \frac{1}{2}\int_{x_0}^{x} \frac{C_{f_0}}{\theta_0} dx - \text{RNS},$$

where the local free-stream velocity is U_∞, momentum thickness θ, displacement thickness δ^*, wall shear stress coefficient C_{f_0} ($= 2\tau_0/\rho U_{\infty_0}^2$), the subscript 0 refers to a reference measurement at $x = x_0$, and RNS is a term representing the contribution from Reynolds normal stresses. RNS was evaluated, and found to contribute at the most 1·8 % to P_R. The results of the momentum balance are shown in figure 5. The agreement is better than found in most adverse gradient experiments.

The models of Perry, Bell & Joubert (1966) and Townsend (1961) were tested on the velocity profiles. Some details of the two models are outlined below.

In their model of boundary layers developing in adverse pressure gradients, Perry *et al.* proposed a two-part layer with a 'wall region' and a 'historical region'. In the wall region, the mean flow behaviour was characterized by the local wall variables, as expressed by

$$U = U(\tau_0, \alpha, \rho, \nu, y),$$

where

$$\alpha = \rho^{-1} dP/dx.$$

In the 'historical region', as the name implies, the upstream history of the layer will affect its shape. The individual component of the 'wall region' mean flow profile were determined by the relative importance of the wall variables in any

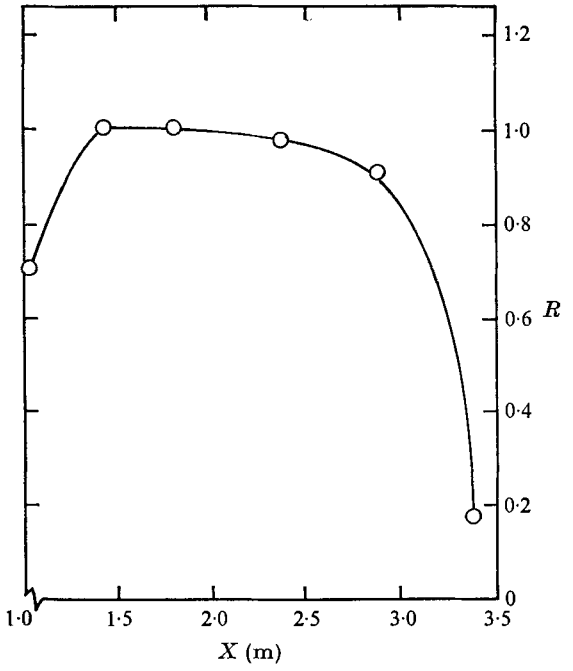

FIGURE 6. Ratio of mean flow inertia to pressure gradient.

$$R = \left(U\frac{\partial U}{\partial x} + V\frac{\partial U}{\partial y}\right)\left(-\frac{1}{\rho}\frac{dP}{dx}\right)^{-1}, \quad \frac{y}{\delta_{99}} = 0{\cdot}1.$$

one region. These hypotheses, together with physical arguments about the flow, led Perry *et al.* to propose three regions in the wall layer (namely, a sublayer, a logarithmic layer and a half-power layer).

The proposed form of the half-power layer was

$$U/U_\tau = K(\alpha y/U_\tau^2)^{\frac{1}{2}} + 1/\kappa \log_e (L_e U_\tau/\nu) + A,$$

where $L_e = CU_\tau^2/\alpha$, K, κ, A and C, are universal constants. L_e is a distance from the wall where the local stress is twice the wall shear stress τ_0 when mean flow inertia forces are negligible. In testing the proposed half-power law, Perry *et al.* discovered that, in the plane of symmetry profiles of Johnston (1957, 1960), there appeared extensive half-power regions, some extending as far as the free stream† (see figure 6 in Perry *et al.*).

It would naturally seem attractive to find a flow situation which could be almost completely characterized by a universal half-power law. To reproduce Johnston's flow conditions, in a 'two-dimensional' sense, the flow had to be subjected to an increasingly adverse pressure gradient. The hypothetical predicted behaviour of such a layer would be a rapid 'thinning out' of both the logarithmic and historical regions, if indeed such regions were observed.

Townsend's (1961) model of the boundary layer was based on a linear stress

† Brown (1971) reasoned that these observations of Perry *et al.* were rather fortuitous.

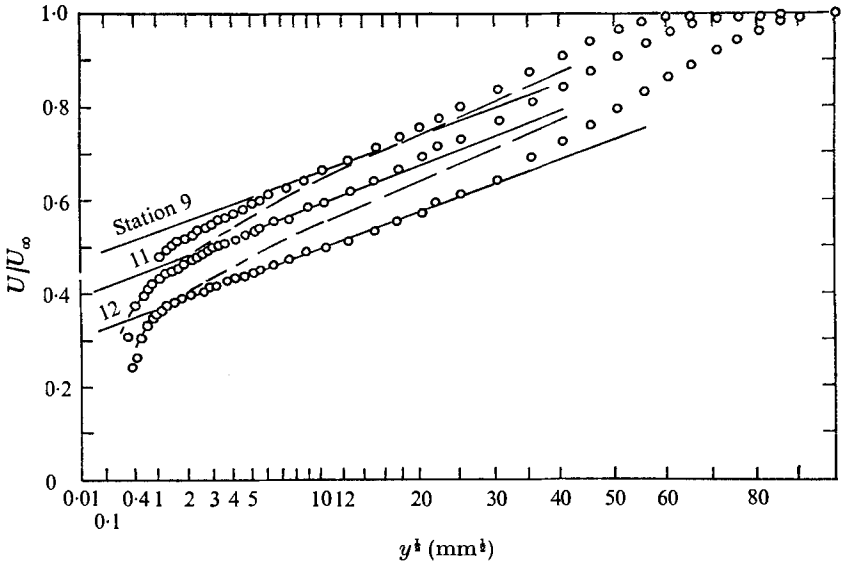

FIGURE 7. Half-power plots. ——, Perry *et al.* (1966) theory ($\kappa = 0{\cdot}4$, $A = 5{\cdot}1$, $C = 0{\cdot}19$; $K = 4{\cdot}16$); – – –, Townsend (1961) theory ($B = 0$).

layer, which implicitly assumes mean flow accelerations independent of distance from the wall. The resulting equation of the mean velocity distribution was given by Townsend as

$$\frac{U}{U_\tau} = \frac{1}{\kappa}\log_e\left[\frac{4U_\tau^3}{\nu a}\frac{[1+ay/U_\tau^2]^{\frac{1}{2}}-1}{[1+ay/U_\tau^2]^{\frac{1}{2}}+1}\right]+A$$
$$-2(1-B)/\kappa+2(1-B)\,[(1+ay/U_\tau^2)^{\frac{1}{2}}/\kappa],$$

where $a = \rho^{-1}\partial\tau/\partial y$ and B is a coefficient related to the spread of turbulent energy by diffusion. In testing the model, several values of B were tried, with $B = 0$ providing the best match to the data. To obtain an estimate of $\partial\tau/\partial y$, the mean flow accelerations were calculated at the outer edge of the logarithmic region. The mean flow acceleration term was found to be of the same order as the pressure gradient term for all but the last two stations 11 and 12 (see figure 6), where the pressure gradient term exceeded the mean flow acceleration term by a factor of approximately five. Consequently, the value of $\partial\tau/\partial y$ used in Townsend's model was $0{\cdot}8\,dP/dx$. The above calculations of mean flow accelerations implied that the shear stress gradient should be approximately zero for all but the last turbulence measuring station T 6. This was later borne out by direct measurement.

The half-power plots for stations 9, 11 and 12 together with the predicted profiles of Townsend and Perry *et al.* are shown on figure 7. As can be seen, neither model is adequate for predicting flow development in the increasingly adverse gradient layer. However, the Perry *et al.* model does predict flow behaviour once d^2P/dx^2 becomes negative.

A further attempt was made to find some characterizing parameter for that part of the layer just outside the logarithmic region. Following the attempts of

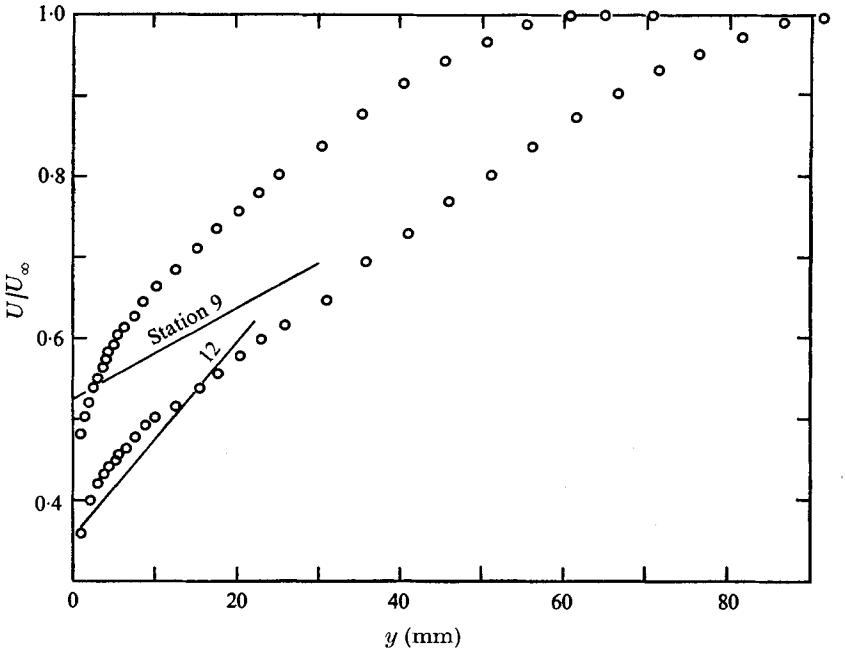

FIGURE 8. Linear law. ——, Perry *et al.* (1966) theory.

Schofield (1969), the local wall shear stress gradient was used in the Perry *et al.* model and again it was found quite inadequate for describing mean flow behaviour.

Perry (1966) extended the regional similarity model of Perry *et al.* to include other history-dependent regions of development in the wall layer. One component of this extended model (linear region) was determined by $d\alpha/dx$. In Perry's layer $d\alpha/dx$ was negative everywhere; and, in the layer reported here, the model was tested for both negative and positive $d\alpha/dx$. The linear plots are shown in figure 8. To present an overall view of development figure 9 shows the plot of δ_{99}, as well as the boundaries of the Perry *et al.* regional similarity model.

For comparison with the behaviour of the distributions of dP/dx and d^2P/dx^2, the non-dimensional parameters $\delta^*(dC_p/dx)/C_{f_0}$ and $\delta^{*2}(d^2C_p/dx^2)/C_{f_0}$ have been calculated for each measuring station. The relevant values, together with other boundary-layer parameters, are listed in table 1.

The velocity profile measurements, taken with round and flat total head tubes, were used to check the displacement effect. The results confirm the findings of McMillan (1956) for round tubes. Young & Maas (1936) took some preliminary measurements with flattened total head tubes, and found that the displacement effect for a rectangular tube was of the same order as that for a round tube of diameter D_r, where D_r is also the height of the rectangular tube in the traverse direction. The present results appear to confirm the conclusion of Young & Maas. The displacement correction for shear was calculated to be of the order of 0·1 mm in y, the distance from the wall, while the displacement correction for the presence of the wall was negligible. The results as presented have not been corrected for these effects.

Station	dC_p/dx (m^{-1})	d^2C_p/dx^2 (m^{-2})	$C_{f_0} \times 10^5$	δ^* ($m \times 10^{-2}$)	$\delta^*(dC_p/dx)/C_{f_0}$	$\delta^{*2}(d^2C_p/dx^2)/C_{f_0}$ ($\times 10^{-9}$)	H	G	PI
1	0·0623	0·0517	279	0·395	0·0882	2·89	1·39	7·55	0·60
2	0·0807	0·0710	268	0·473	0·142	5·93	1·39	7·64	0·63
3	0·102	0·0732	250	0·539	0·219	8·51	1·39	7·78	0·72
4	0·127	0·0771	237	0·604	0·323	11·9	1·39	7·86	0·72
5	0·152	0·108	213	0·744	0·531	28·1	1·40	8·25	0·83
6	0·169	0·140	204	0·811	0·672	45·1	1·41	8·44	0·85
7	0·196	0·207	188	0·875	0·912	84·3	1·43	8·95	1·1
8	0·240	0·390	167	1·02	1·47	243	1·44	9·43	1·2
9	0·295	0·161	151	1·19	2·32	277	1·46	9·96	1·3
10	0·301	0	135	1·30	2·90	0	1·48	10·6	1·5
11	0·288	−0·115	112	1·51	3·88	−234	1·51	11·6	1·8
12	0·226	−0·202	68·5	2·34	7·72	−1614	1·61	15·2	2·9

TABLE 1. Values of non-dimensional parameters $\delta^*(dC_p/dx)/C_{f_0}$ and $\delta^{*2}(d^2C_p/dx^2)/C_{f_0}$, together with other boundary-layer parameters. Shape factor $H = \delta^*/\theta$, where θ = local momentum thickness, equilibrium shape factor $G = (2/C_f')^{\frac{1}{2}}[1 - 1/M]$, Coles' wake parameter PI as found from $(2/C_f')^{\frac{1}{2}} = 1/0{\cdot}4\,[\log_e(\delta_{99}U_\tau/\nu) + 2{\cdot}04 + 2(\mathrm{PI})]$, given by Coles & Hirst.

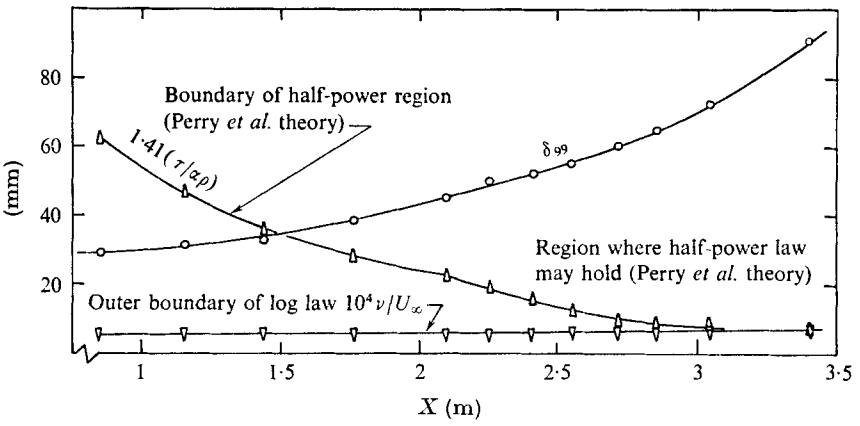

FIGURE 9. Overall view of development.

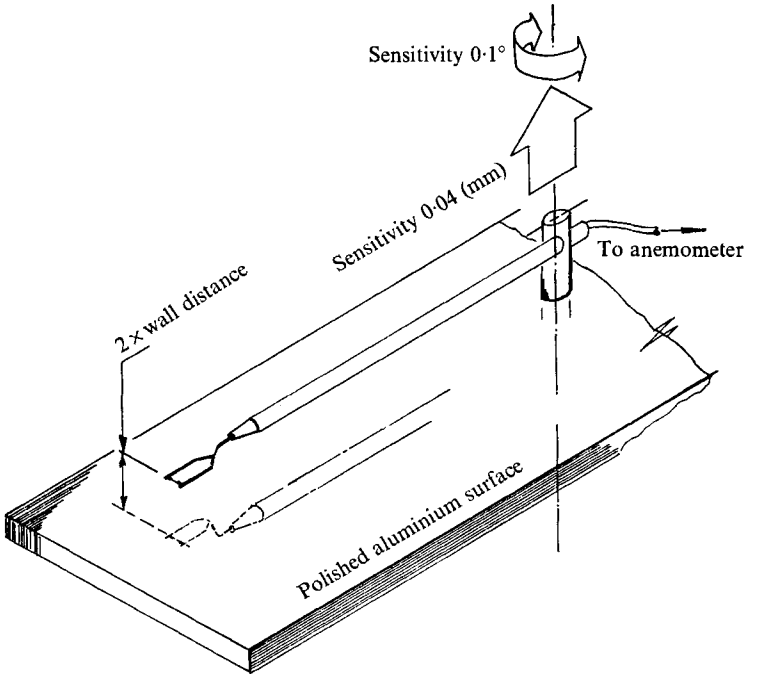

FIGURE 10. Schematic view of traverse with normal wire in measuring position.

4. Turbulence measurements: the procedure

In this work, normal wire probes were used for u_1 measurement, while single inclined wire probes, together with the u_1 information measured, were used for evaluating $(\overline{u_2^2})^{\frac{1}{2}}$, $(\overline{u_3^2})^{\frac{1}{2}}$ and $\overline{u_1 u_2}$. The general response equations for an inclined wire in a plane flow field are given by Samuel (1973). All various sensitivites were measured by direct dynamic calibration. The details of the calibration procedures

Turbulence measuring station	Downstream distance, x (m)	Mean flow measuring station	Downstream distance, x (m)
T 1	1·04	2	1·16
T 2	1·44	3	1·44
T 3	1·79	4	1·76
T 4	2·38	7	2·40
T 5	2·89	10	2·87
T 6	3·39	12	3·40

TABLE 2. Downstream positions of turbulence stations, together with nearest corresponding mean flow station.

are given by Morrison *et al.* (1972) and Perry & Morrison (1971*a*). The hot-wire anemometer used was a Melbourne University Constant-Temperature Anemometer (the performance of this device was analysed by Perry & Morrison 1971*b*).

Turbulence measurements were taken using a specially designed traverse, to provide accurate positioning, with reliable repeatability and without the need to re-zero the probe during a traverse. The traverse was fitted to measuring stations rigidly attached to the tunnel floor. For the inclined wire measurements a specially designed rotating head mechanism was used. The position of the wire relative to the tunnel floor was found by sighting the wire and its reflexion in the polished wall through a telescope equipped with a calibrated graticule. The traverse and a normal wire in the measuring position near the wall are shown schematically in figure 10.

The turbulence measuring stations T 1 to T 6 are also shown in figure 3; and table 2 lists the downstream positions of both the turbulence stations, as well as the nearest corresponding mean flow measuring station. It is clear that, apart from station T1 (which lies between stations 1 and 2 in an almost zero pressure gradient region), the greatest discrepancy between the turbulence measuring stations and the corresponding mean flow station is 30 mm. Quadratic interpolation was used to obtain the mean velocity profile at each turbulence measuring station from the Pitot traverses. The interpolated profiles are shown in figure 11.

4.1. *Turbulence intensities*

At each measuring station the following measuring procedure was adopted. (i) A normal hot wire was calibrated dynamically for two resistance ratios 1·5 and 2·0. (ii) $(\overline{u_1^2})^{\frac{1}{2}}$ profiles were measured for the two resistance ratios 1·5 and 2·0. (iii) The wire was recalibrated dynamically at both resistance ratios. (iv) If either the calibrations disagreed, or the profiles at the two resistance ratios were different, the results were discarded and the process repeated. (v) A single inclined wire was calibrated dynamically for both transverse and longitudinal fluctuations. (vi) e_1, e_2 and e_3 were measured at positions through the layer, using the traverse and the rotating head mechanism, where e_1, e_2, e_3 components and their relationship to the flow co-ordinates are shown in figure 12. (vii) The wire was recalibrated dynamically. (viii) If the calibrations disagreed the results were discarded, and steps (v)–(vii) were repeated.

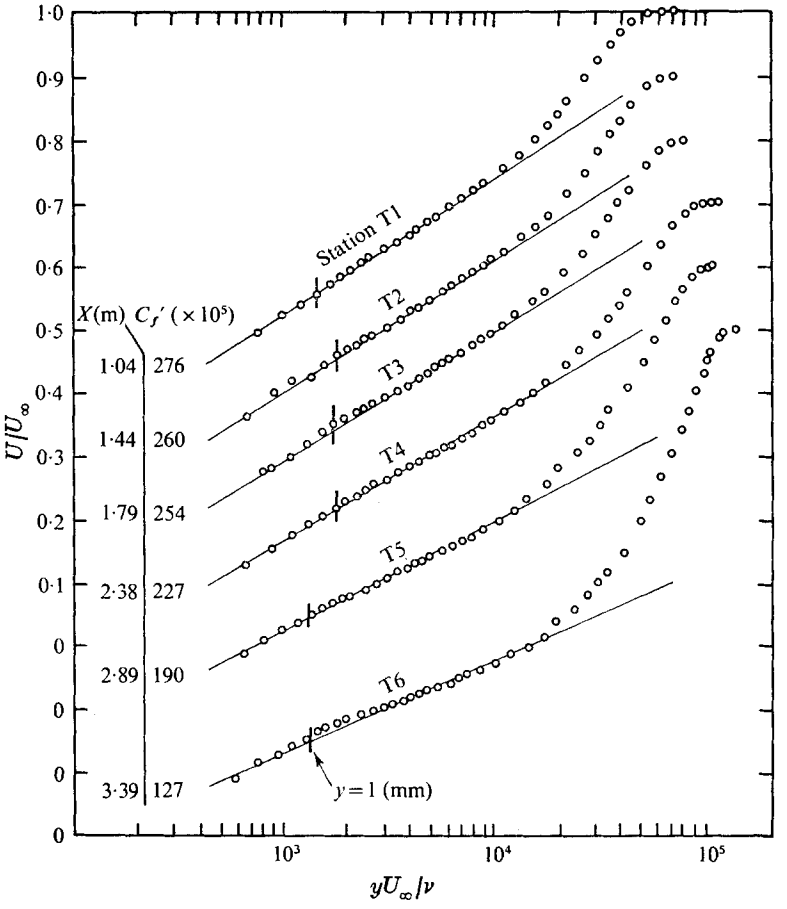

FIGURE 11. Mean velocity profiles interpolated from Pitot measurements. $C_f' = 2\tau_0/\rho U_\infty^2$. ——, Clauser lines ($\kappa = 0{\cdot}4$, $A = 5{\cdot}1$).

The wire material used was platinum (Wollaston wire), with a sensing element of diameter 4 μm and 1 mm long. Typical wire cold resistance was 9 Ω. For inclined wires, a typical wire angle was 40–50°; but, owing to wire curvature in the plane of measurement caused by thermal expansion or manufacturing uncertainties, the notion of wire angle seems to be somewhat academic.

The normal intensities $(\overline{u_2^2})^{\frac{1}{2}}$, $(\overline{u_3^2})^{\frac{1}{2}}$ and Reynolds (kinematic) shear stress term $\overline{u_1 u_2}$ were evaluated using the three sets of measurements taken with the inclined wire, together with the previously measured $(\overline{u_1^2})^{\frac{1}{2}}$. All the profiles and calibration curves were carefully matched for temperature; details of the correction scheme are given by Samuel (1973).

4.2. *Spectra*

Energy spectra were measured at two streamwise positions, $x = 1{\cdot}62$ m and $x = 3{\cdot}7$ m. For both positions, several power spectral density profiles were plotted through the boundary-layer. The instrument used was a B & K type

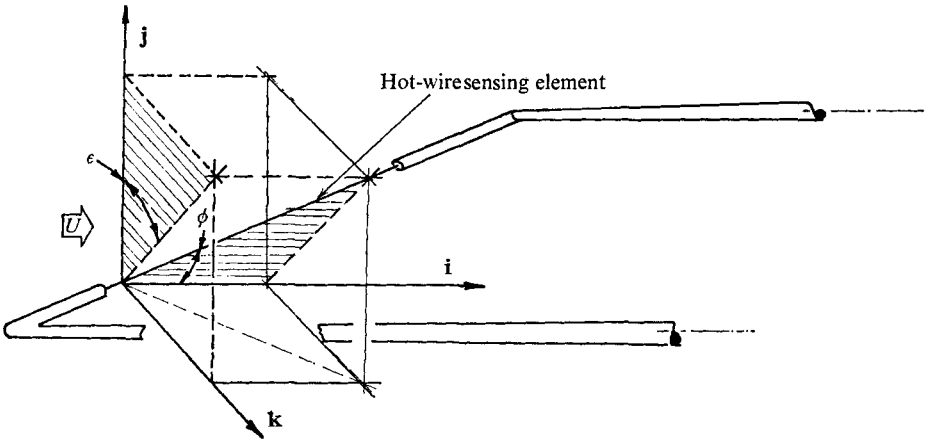

FIGURE 12. Nomenclature for inclined wire data. $\mathbf{V} = (\bar{U}+u_1')\mathbf{i}+u_2'\mathbf{j}+u_3'\mathbf{k}$, $e_n = f(\phi,\epsilon)$, $e_1 = f(\phi,0) = Au_1'+Bu_2'$, $e_2 = f(\phi,\pi) = Au_1'-Bu_2'$, $e_3 = f(\phi,\frac{1}{2}\pi) = Au_1'+Bu_3'$.

2107 constant percentage bandwidth frequency analyser, and an Electronics Associates Inc. type TR 20 analog computer for r.m.s. measurements of the output signal. The frequency analyser was calibrated using a BWD Model 112 sine wave generator. Both ends of each frequency range were calibrated, and linear calibration was assumed between these end points. All measurements were corrected using the calibration curve thus obtained.

5. Results of the turbulence measurements

5.1. *Shear stress profiles*

The distribution of $\overline{u_1u_2}$ can be calculated in that region of the layer where the law of the wall is valid. The calculation follows Coles (1955), who derived

$$-\frac{\overline{u_1u_2}}{U_\tau^2} = 1-\frac{df}{dz}+\frac{y}{\tau_0}\frac{dP}{dx}-\frac{\nu}{\lambda U_\tau}\int_0^z f^2(z)\,dz,$$

where dP/dx is the streamwise pressure gradient, and

$$f = U/U_\tau, \quad z = yU_\tau/\nu, \quad -1/\lambda = U_\tau^{-1}(dU_\tau/dx).$$

The above equation may be cast into the following form, involving mostly non-dimensionalized coefficients:

$$-\frac{\overline{u_1u_2}}{U_{\infty_0}^2} = \tfrac{1}{2}C_{f_0}\left[1-\frac{df}{dz}+\frac{z\sqrt{2}}{R_eC_{f_0}^{1.5}}\frac{dC_p}{dx}+\frac{1}{\sqrt{2}\,R_eC_{f_0}^{1.5}}\frac{dC_{f_0}}{dx}\int_0^z f^2\,dz\right],$$

where U_{∞_0} is the reference mean velocity,

$$C_{f_0} = 2\tau_0/\rho U_{\infty_0}^2, \quad C_p = (P-P_0)/\tfrac{1}{2}\rho U_{\infty_0}^2 \quad \text{and} \quad Re = U_{\infty_0}/\nu.$$

Table 3 shows the various parameters associated with each measuring station, where U_∞ is the local free-stream velocity. The measured Reynolds stress distributions are shown in figures 13 (*a*) and (*b*), together with the calculated values for

Station	Downstream distance (m)	C_{f_0} ($\times 10^{-3}$)	U_∞ ($m\,s^{-1}$)	dC_p/dx ($m^{-1} \times 10^{-2}$)	$-dC_{f_0}/dx$ ($m^{-1} \times 10^{-4}$)	$U_\tau^3/\alpha\nu$
T 1	1·04	2·75	26·3	7·55	3·18	2300
T 2	1·44	2·50	26·1	10·25	6·53	1460
T 3	1·79	2·37	25·4	12·7	7·65	1056
T 4	2·38	1·88	24·9	19·6	9·66	481
T 5	2·89	1·35	22·2	30·2	{11·62 13·70}	193
T 6	3·39	0·68	19·7	22·6	{13·70 9·66 7·65}	94·1

TABLE 3. Parameters associated with each measuring station. U_∞ is the local free-stream velocity.

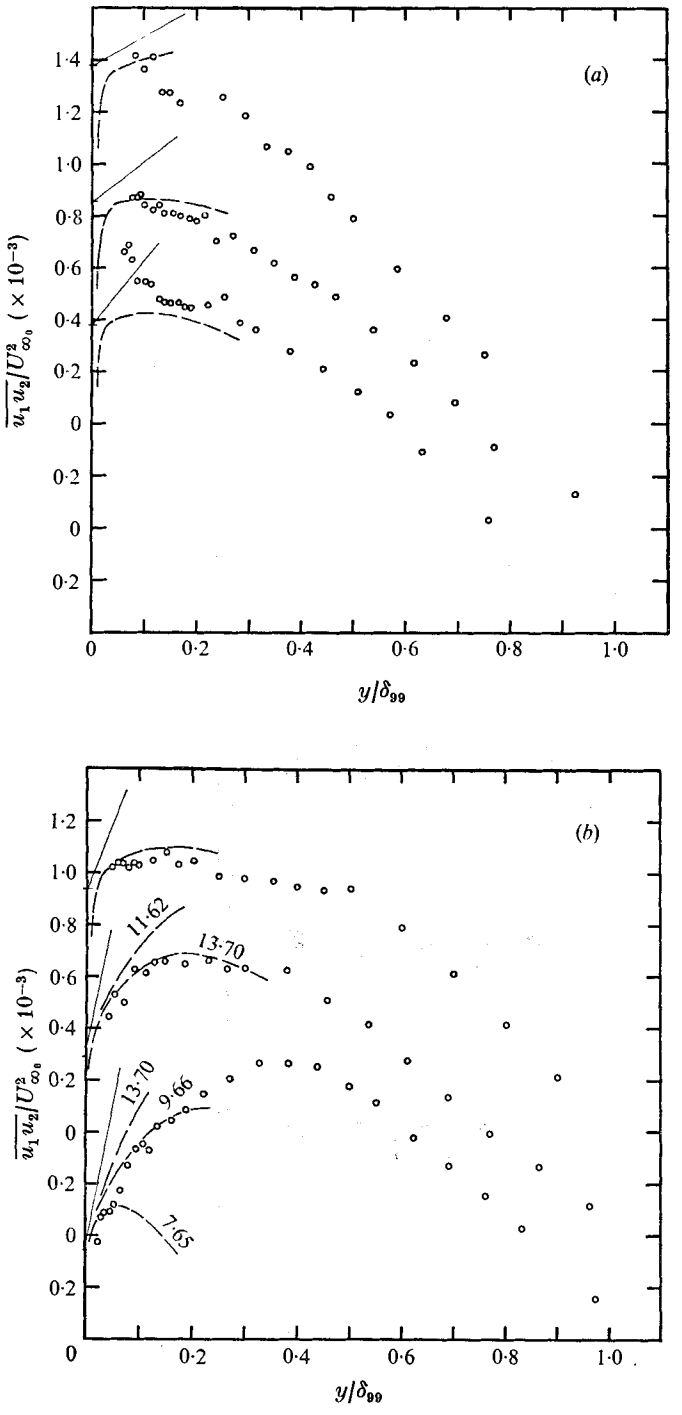

FIGURE 13. Reynolds shear stress profiles. ——, lines corresponding to local dP/dx (i.e. slope $\frac{1}{2}\delta_{99}\,dC_p/dx$); – – –, Coles' (1955) equation. Profiles in order from top: (*a*) T 1–T 3; (*b*) T 4–T 6. Numbers on predicted profiles correspond to value of dC_{f_0}/dx used in calculation.

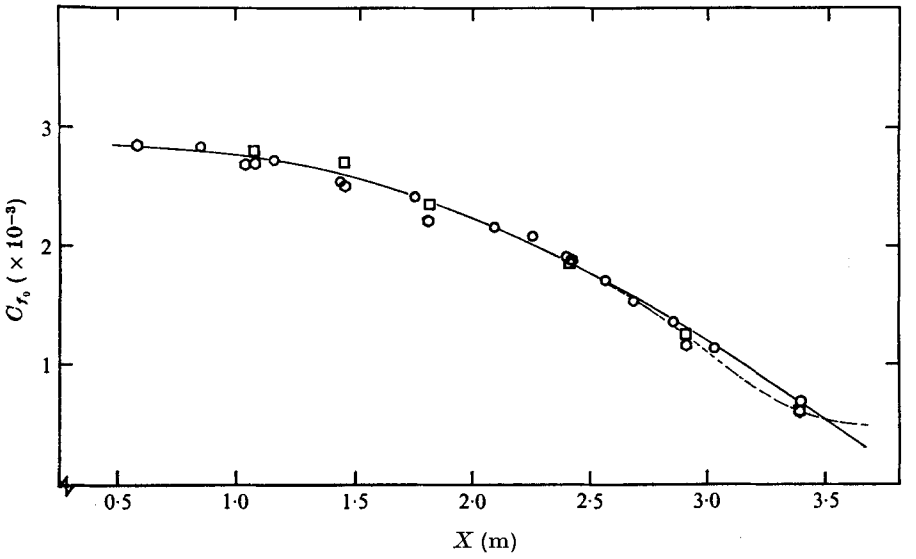

FIGURE 14. Wall shear stress distribution. ○, mean flow (Clauser lines); □, floating element; ◊, Preston tubes; ——, conjectured line of best fit; – – – –, dC_{f_0}/dx from this line provide best match of Coles equation with data (figure 16(*b*)).

the inner 20 % of the layer. The values of local wall shear stress gradients, used in the calculation, were found by graphical differentiation of the wall shear stress distribution, shown in figure 14.

To check the form of the wall shear stress distribution, the local Reynolds stress distribution was calculated for several values of wall shear stress gradient at the doubtful points. The best match between measured and calculated Reynolds stress distributions was accepted as corresponding to the correct wall shear stress gradient.

For comparison the local pressure gradient term, appropriately normalized to give $\frac{1}{2}\delta_{99}\, dC_p/dx$, is shown in figures 13(*a*) and (*b*). Although the stress distribution is nowhere linear, the stress gradient $\partial\tau/\partial y$ tends to the local pressure gradient at station T 6, as it should, since the mean flow accelerations are small there.

Many calculation methods for predicting boundary-layer behaviour are based on the hypothesis of a 'universal' eddy-viscosity distribution. Universality in this context refers to the assumption that the local variables U_τ, U_∞, dP/dx and $\partial U/\partial y$ completely determine the eddy-viscosity distribution and consequently the Reynolds shear stress distribution. This assumption needs to be tested. If the assumption(s) are shown to be invalid, then doubt is cast on the method, whether or not it still manages to predict the layer to a certain degree of accuracy.

The model of Cebeci & Smith is typical of all such models; but it contains the refinement of matching the physical conditions at both the wall and outer regions of the layer. This model was chosen for comparison with the measured shear stress distribution in the increasingly adverse gradient layer. Some details of the model are given below.

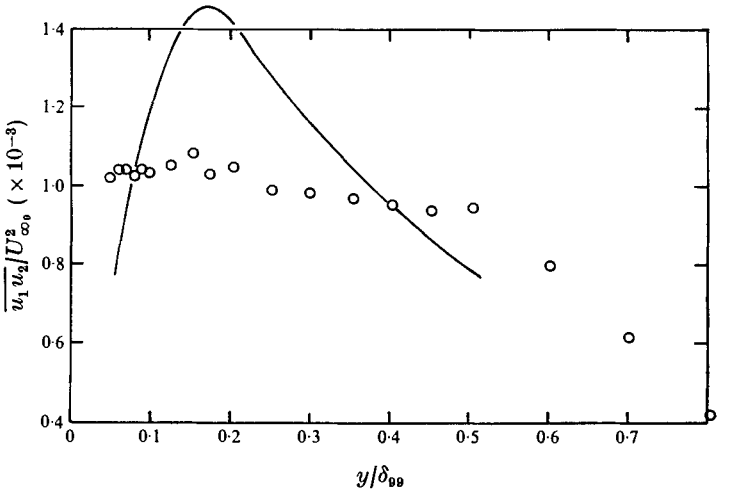

FIGURE 15. Eddy-viscosity model prediction of Reynolds shear stress. ○, measurements at station T 4; ——, Cebeci & Smith (1968) model.

5.2. *Inner eddy-viscosity distribution*

In this region the eddy viscosity is obtained from a model, which states that

$$\epsilon_i = l^2 |\partial U/\partial y|,$$

where ϵ_i is the eddy viscosity and l is a length proportional to distance from the wall

$$l = \text{constant} \times y,$$

where the constant is usually taken as the von Kármán constant κ.

To match the boundary condition near the wall, Cebeci & Smith modified Van Driest's (1956) viscous sublayer model to account for effects of pressure gradient. The resulting expression for eddy viscosity is given by

$$\epsilon_i = \kappa^2 y^2 \{1 - \exp\{-y/26\nu[(U_\tau^2 + \alpha y)]^{\frac{1}{2}}\}\}^{\frac{1}{2}} |\partial U/\partial y|.$$

5.3. *Outer eddy-viscosity distribution*

The usual assumption of constant outer eddy viscosity was modified by Cebeci & Smith, using an empirical intermittency distribution derived from the zero pressure gradient measurements of Klebanoff (1955), yielding

$$\epsilon_0 = K_2 U_\infty \delta^* [1 + 5{\cdot}5(y/\delta)^6]^{-1},$$

where K_2 is given by Cebeci & Smith as 0·0186. The two eddy-viscosity distributions were matched at the point in the boundary layer where $\epsilon_i = \epsilon_0$.

Calling the total distribution, made up of ϵ_i and ϵ_0, ϵ, the shear stress at any point in the layer is

$$\tau = \epsilon(\partial U/\partial y).$$

This last expression was evaluated for the increasingly adverse pressure gradient layer, at all the T stations (with $\kappa = 0{\cdot}4$ and $K_2 = 0{\cdot}0168$), the results were nor-

malized with $U^2_{\infty_0}$, and compared with the measured shear stress distributions. At each position y in the layer, the local $\partial U/\partial y$ was evaluated from the differential of a smooth quadratic fitted to five points distributed about y. However, even with this involved process of differentiation, the results were somewhat scattered.

A typical shear stress distribution is shown in figure 15, where the predicted distribution has been hand smoothed to obtain a line of best fit. As can be seen, the fit to the measured data is poor, and this condition prevails throughout the layer.

5.4. *Normal turbulence intensities*

$(\overline{u_1^2})^{\frac{1}{2}}$, $(\overline{u_2^2})^{\frac{1}{2}}$ and $(\overline{u_3^2})^{\frac{1}{2}}$ distributions are shown in figures 16(*a*)–(*c*), respectively. These plots appear to follow the trends reported elsewhere in the literature. All have been normalized by the reference mean velocity U_{∞_0}. The y ordinate was normalized by δ_{99}, obtained from a faired in curve of the measured δ_{99} distribution along the measuring plate. As can be seen from figure 16(*a*), the outer 80 % of the $(\overline{u_1^2})^{\frac{1}{2}}$ profiles are very similar for the increasingly adverse gradient layer (stations T 2–T 5 inclusive, shown shaded). This implies that the rate of increase of turbulence level $(\overline{u_1^2})^{\frac{1}{2}}/U$ is not as great as that observed in a decreasingly adverse gradient layer.

In the region $0 < y/\delta_{99} < 0{\cdot}2$, $(\overline{u_1^2})^{\frac{1}{2}}/U_\infty$ is approximately constant between 7·5–8 %, and its magnitude decreases with downstream distance. For this first 20 % of the layer, $(\overline{u_1^2})^{\frac{1}{2}}/U_\tau$ lies in the range 2·25 (T 1) to 3·68 (T 6). The first value agrees well with that observed by Klebanoff in a zero pressure gradient layer. The outer portion of the profiles are a function of y/δ_{99}.

The profile corresponding to station T 1 is essentially in a zero pressure gradient. It closely approximates the shape of Klebanoff's data. At station T 6, the pressure gradient was decreasingly adverse. The $(\overline{u_1^2})^{\frac{1}{2}}$ profile measured here is significantly different from the profiles in the increasingly adverse pressure gradient, which lie between stations T 1 and T 5. This rather significant change in a relatively short development length is associated with the rapid thickening of the layer in this region (see figure 9). The reasons for such rapid redistribution of turbulence intensity are difficult to state without further evidence. Any reference to the sign of d^2P/dx^2 is mere conjecture; but the difference in the sign of d^2P/dx^2 was the most significant difference between conditions at stations T 5 and T 6.

As stated above, the $(\overline{u_1^2})^{\frac{1}{2}}$ intensities were measured at two resistance ratios, $R = 2$ and 1·5. Perry & Morrison (1971*c*) proposed the possibility of self-induced wire signal errors due to filament vibration when measurements are made in 'peaky' spectrum turbulence. Furthermore, they showed that the magnitude of a self-induced signal is related to the bowing of the measuring element. Since the wire bows significantly more for a resistance ratio of 2 compared with 1·5, the two sets of measurements provided some indication of a self-induced signal if this existed in the broad spectrum turbulence.

Figure 17 shows that any self-induced signal due to wire vibration was negligible. Both plots of $(\overline{u_1^2})^{\frac{1}{2}}$, measured with different resistance ratios, are in good agreement.

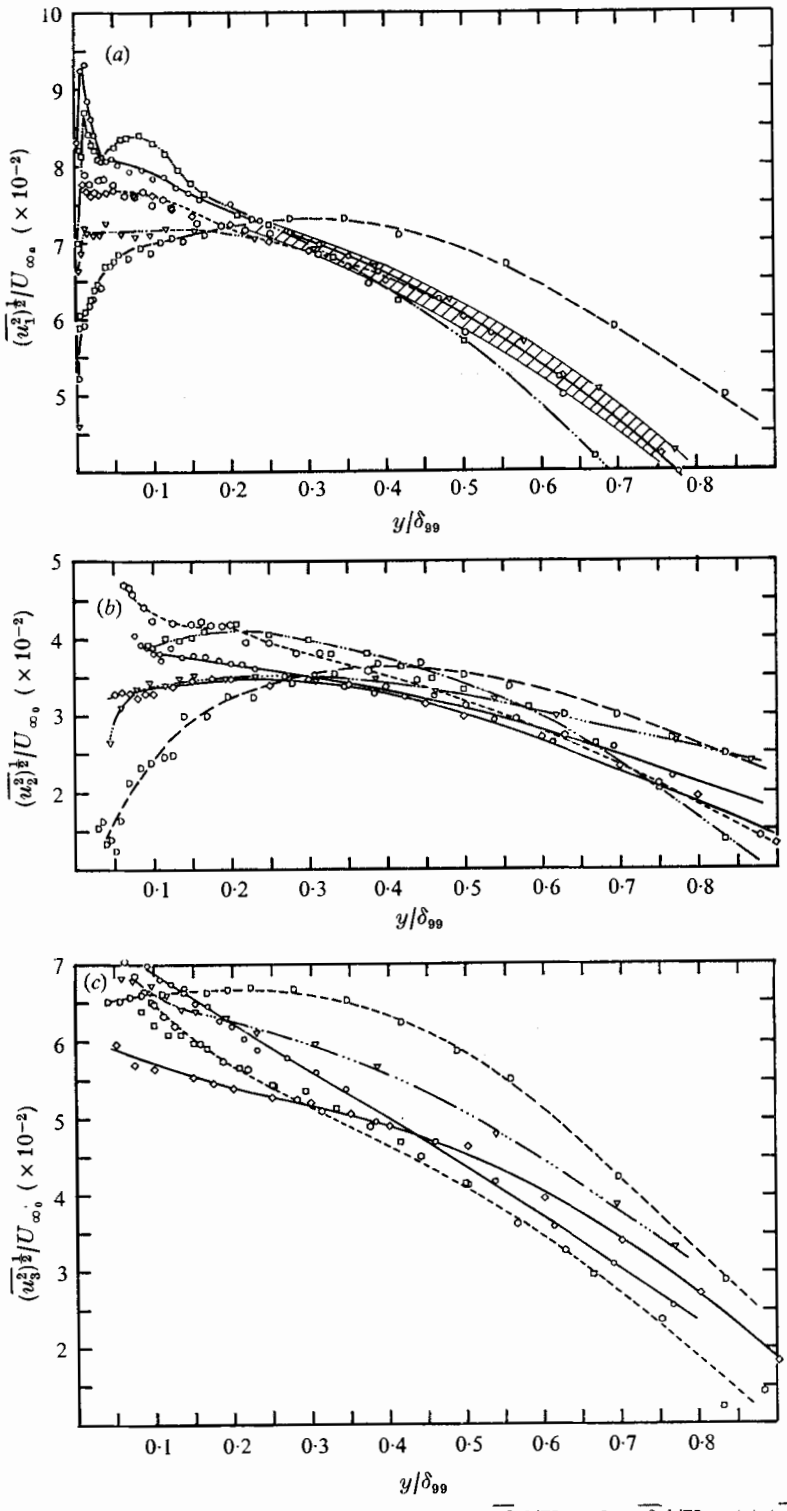

FIGURE 16. Turbulence intensity profiles: (*a*) $(\overline{u_1^2})^{\frac{1}{2}}/U_{\infty_0}$, (*b*) $(\overline{u_2^2})^{\frac{1}{2}}/U_{\infty_0}$, (*c*) $(\overline{u_3^2})^{\frac{1}{2}}/U_{\infty_0}$. □, T 1; ○, T 2; ◊, T 3; ◇, T 4; ▽, T 5; ▢, T 6.

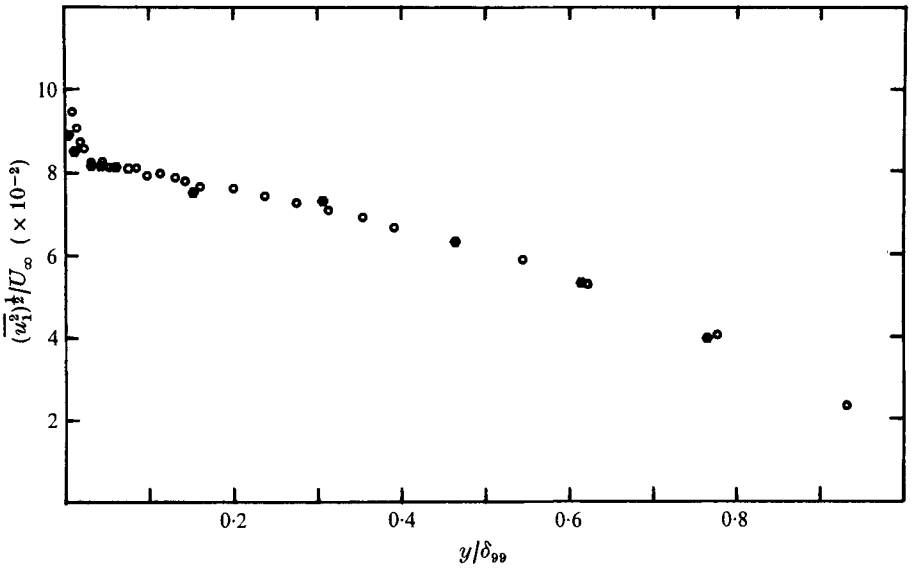

FIGURE 17. $(\overline{u_1^2})^{\frac{1}{2}}$ measured at station T 3 with the same wire at two resistance ratios: ○, 1·5; ●, 2·0.

5.5. *Spectra*

Streamwise component $(\overline{u_1^2})^{\frac{1}{2}}$ energy spectra were measured at two stations T 1 and T 4, to provide a representative picture of spectral energy distribution in the increasingly adverse gradient layer. Measurements were taken at three positions in the layer at both of the stations. The three positions were chosen to fall inside the viscous region, the logarithmic region and outer region, respectively.

The spectra were plotted as $\omega E(\omega)$ *vs.* $\log \omega$ (figures 18 (*a*) and (*b*)) to emphasize the differences between measurements very near the wall and those taken some distance away. In the range 150 Hz–1 kHz, a significantly greater area (and hence energy) appears for the profiles taken near the wall at both stations T 1 and T 4. The excess energy causes a slight bump in the spectrum near 300 Hz, which was first thought to be a characteristic of the sublayer. But it was established that this feature was due to wire and support vibration. The broad-band signal from the wire at six wire diameters from the wall under these conditions is shown in figure 19. It seems probable that the mechanically induced vibrations in the wire and support resulted in periodic variation in conduction to the wall. As shown by the spectra, this effect seems to persist for twenty-five to thirty wire diameters from a wall which is a good conductor. It was not possible to reproduce this phenomenon over an insulating wall. Consequently, little or no reliance may be placed on turbulence measurements taken within 30 wire diameters of a conducting wall. The measurements taken nearest the wall have been excluded from figure 20, which shows the energy spectra plotted in the conventional form of $E(k)$ against k, where the wavenumber

$$k = \omega/U_\infty \ (\mathrm{m}^{-1}), \quad E(k) = \omega E(\omega)/k \ (\mathrm{m})$$

and U_∞ is the local mean velocity.

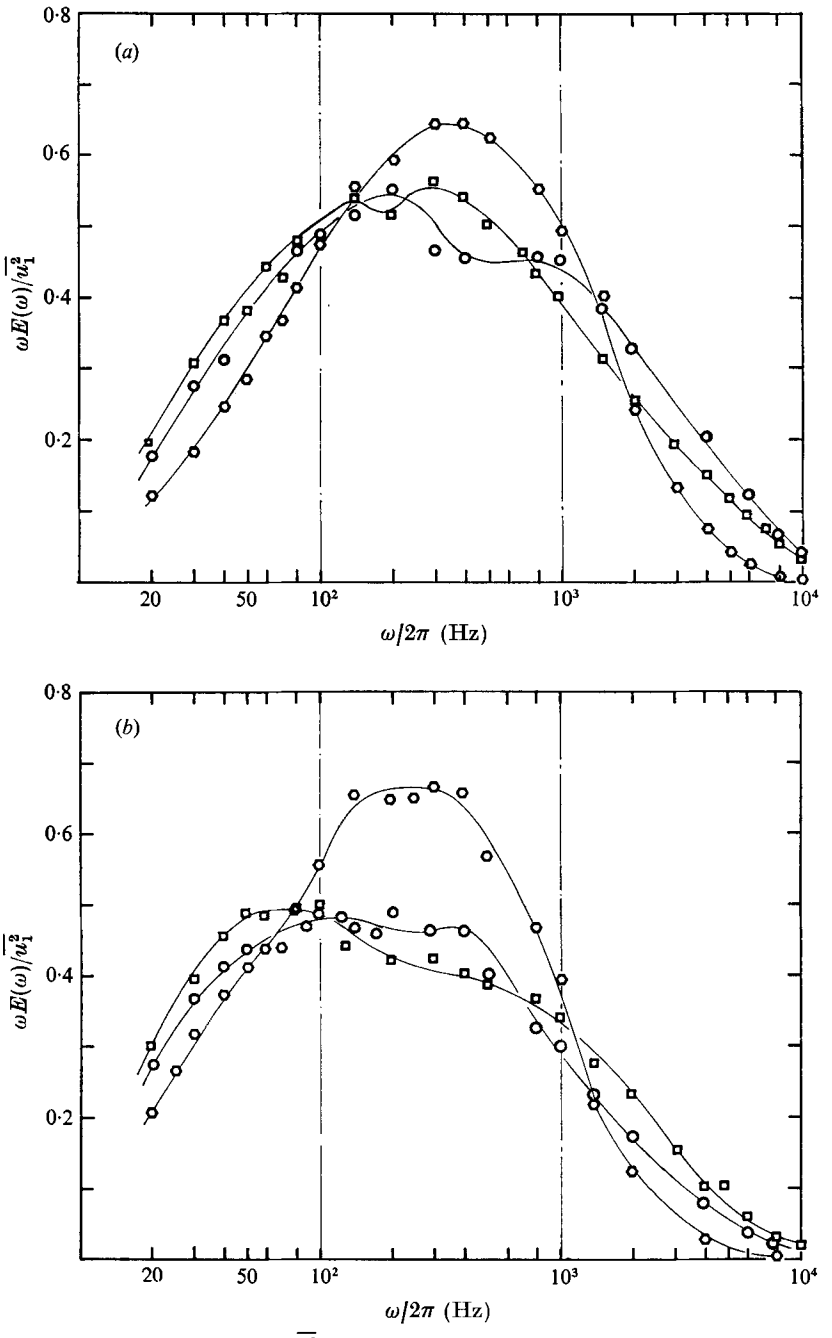

FIGURE 18. $(\overline{u_1^2})^{\frac{1}{2}}$ energy spectra. ——, faired curve.

	y/δ_{99} ($\times 10^{-2}$)	
	(*a*) T 1	(*b*) T 4
◇	0·42	0·25
○	2·1	2·5
□	4·2	15

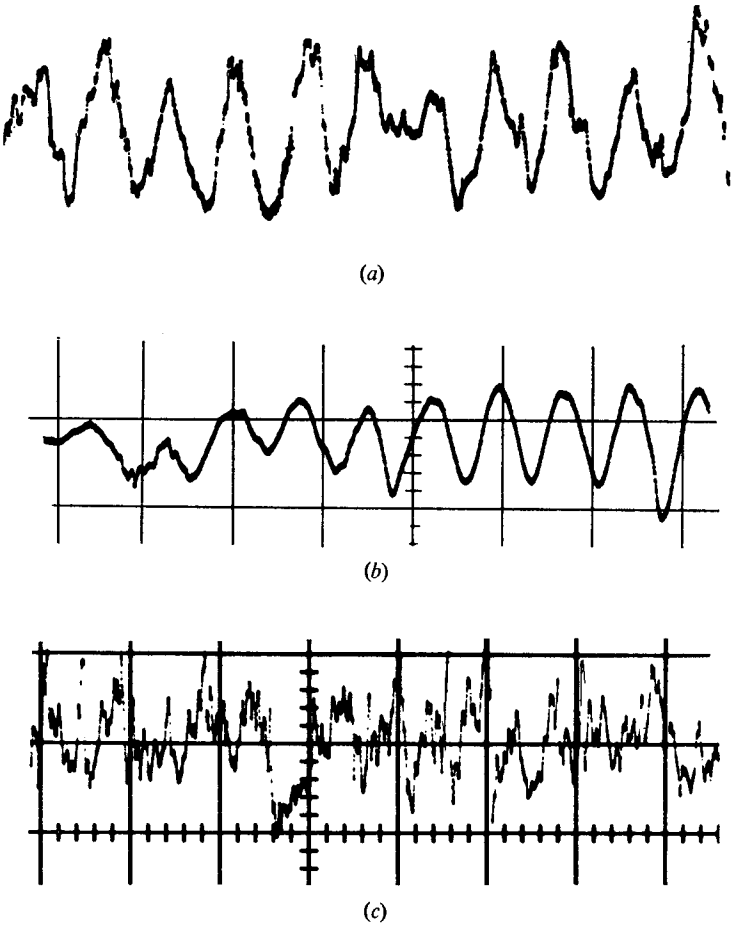

FIGURE 19. Hot-wire output time traces, exhibiting vibration-induced conduction to wall. Wire at (*a*) 0·025 mm from wall, (*b*) the same with sensing element covered to remove signal due to wind, (*c*) 0·08.

The plots appear to follow the trend found elsewhere in the literature (see e.g. Klebanoff 1954; Klebanoff & Diehl 1952). The energy in the small-wavenumber range falls off as the wall is approached, and the large portion of energy production is due to eddies in the wavenumber range $0{\cdot}005\,\mathrm{m}^{-1} < k < 0{\cdot}05\,\mathrm{m}^{-1}$.

6. Comments and conclusions

Mean flow

(i) The mean velocity profiles in the region near the wall gave excellent agreement with the logarithmic law of the wall.

(ii) Wall shear stress measurements were taken using Preston tubes, a floating element meter and a Clauser chart. The results from all three methods are in excellent agreement.

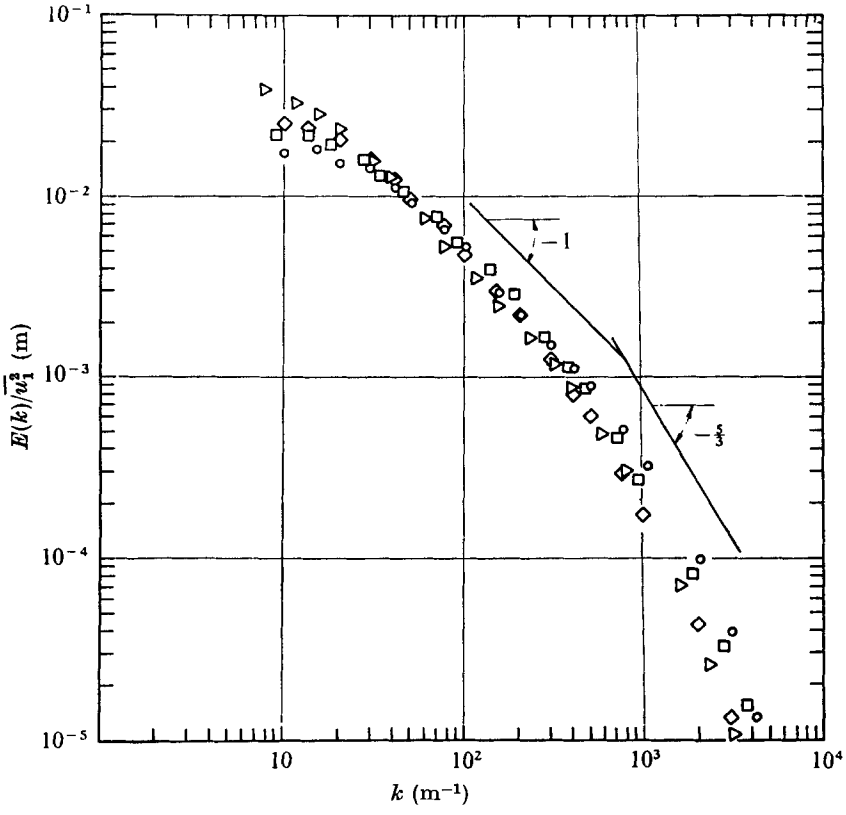

FIGURE 20. Energy spectra.

	Station	y/δ_{99}
○	T 1	0·021
□	T 1	0·042
◇	T 4	0·025
▷	T 4	0·15

(iii) The models of Perry *et al.*, Perry and Townsend, used for predicting the development of the outer parts of the layer, gave disappointing results.

All these models were previously tested in flow situations where the mean flow acceleration was much smaller than the local kinematic pressure gradient. In the layer reported here, these terms were of the same order at the outer edge of the logarithmic law, and this may be the reason why the models failed. Furthermore, Townsend's model rests on the hypothesis of a constant shear stress gradient (linear stress layer), requiring rather stringent conditions for its existence. Consequently, the failure of the model is not surprising, as none of the shear stress profiles exhibited linear regions.

Turbulence measurements

(iv) The distributions of shear stress in the wall region show some agreement with values calculated by Coles' method.

(v) The simple form of universal eddy-viscosity distribution, represented by

the model of Cebeci & Smith, fails more or less drastically in this layer. Perhaps this failure, and naturally the inferred failure of all similar models, is due to the simple assumptions on which the model rests. However, until a satisfactory model is formulated, the use of all eddy-viscosity models must be treated with scepticism.

(vi) The spectra measurements suggest that turbulence measurements taken very close to conducting walls (less than 30 wire diameters) should be viewed with some caution.

General

Since all the tested models, apart from the law of the wall, failed in the increasingly adverse pressure gradient layer, any calculation procedure based on such models should be avoided.

REFERENCES

ABBOTT, I. H. & VON DOENHOFF, A. E. 1949 *Theory of Wing Sections*. McGraw-Hill.

BRADSHAW, P. 1965 *NPL Aero. Rep.* no. 1171.

BROWN, K. C. 1971 Ph.D. thesis, University of Melbourne.

BROWN, K. C. & JOUBERT, P. N. 1969 *J. Fluid Mech.* **35**, 737.

CEBECI, T. & SMITH, A. M. O. 1968 *McDonnel-Douglas Rep.* DAC-67130.

CLAUSER, F. H. 1954 *J. Aero. Sci.* **21**, 91.

COLES, D. 1955 50 *Jahre Grenzschichtforschung* (ed. H. Gortler and W. Tollmien), p. 153. Braunschweig: Vieweg.

COLES, D. & HIRST, E. (ed.) 1968 *AFOSR-IFP-Stanford Conf.* vol. 2.

GOLDSTEIN, S. (ed.) 1965 *Modern Developments in Fluid Dynamics*, vol. 2. Dover.

HOLT, B. W. 1969 M. Eng. Sci. thesis, University of Melbourne.

JOHNSTON, J. P. 1957 *M.I.T. Gas Turbine Lab. Rep.* no. 39.

JOHNSTON, J. P. 1960 *Trans. A.S.M.E.* D **82**, 622.

KLEBANOFF, P. S. 1954 *N.A.C.A. Rep.* no. 3178.

KLEBANOFF, P. S. 1955 *N.A.C.A. Rep.* no. 1247.

KLEBANOFF, P. S. & DIEHL, Z. W. 1952 *N.A.C.A. Rep.* no. 1110.

KLINE, S. J., MORKOVIN, M. V., SOVRAN, G. & COCKRELL, D. J. (ed.) 1968 *AFOSR-IFP-Stanford Conf.* vol. 1.

MCMILLAN, F. A. 1956 *Aero. Res. Counc. R. & M.* no. 3028.

MORRISON, G. L., PERRY, A. E. & SAMUEL, A. E. 1972 *J. Fluid Mech.* **52**, 465.

MOSES, H. L. 1964 *MIT Gas Turbine Lab. Rep.* no. 73.

PATEL, V. C. 1965 *J. Fluid Mech.* **23**, 185.

PERRY, A. E. 1966 *J. Fluid Mech.* **26**, 481.

PERRY, A. E., BELL, J. B. & JOUBERT, P. N. 1966 *J. Fluid Mech.* **25**, 299.

PERRY, A. E. & MORRISON, G. L. 1971*a* *J. Fluid Mech.* **47**, 577.

PERRY, A. E. & MORRISON, G. L. 1971*b* *J. Fluid Mech.* **47**, 765.

PERRY, A. E. & MORRISON, G. L. 1971*c* *J. Fluid Mech.* **50**, 815.

PERRY, A. E., SCHOFIELD, W. H. & JOUBERT, P. N. 1969 *J. Fluid Mech.* **37**, 383.

SAMUEL, A. E. 1973 Ph.D. thesis, University of Melbourne.

SANDBORN, V. A. & SLOGAR, R. J. 1955 *N.A.C.A. Tech. Note*, no. 3264.

SCHOFIELD, W. H. 1969 Ph.D. thesis, University of Melbourne.

STRATFORD, B. S. 1959*a* *J. Fluid Mech.* **5**, 1.

STRATFORD, B. S. 1959*b* *J. Fluid Mech.* **5**, 17.

TOWNSEND, A. A. 1961 *J. Fluid Mech.* **11**, 97.

VAN DRIEST, E. R. 1956 *J. Aero Sci.* **23**, 1007.

YOUNG, A. D. & MAAS, J. N. 1936 *Aero. Res. Counc. R. & M.* no. 1770.